



Investigation of Tensile Flow Behavior of Al–Mg Alloy at Warm Temperature: Constitutive Modelling and Microstructural Evolution

Shahin Ahmad^{1,3} · Alankar Alankar² · Vilas Tathavadkar³ · K. Narasimhan¹

Received: 26 September 2023 / Accepted: 26 December 2023 / Published online: 6 February 2024
© The Author(s) under exclusive licence to The Korean Institute of Metals and Materials 2024

Abstract

The flow behavior of the AA5052 alloy in a fully annealed state was analyzed across a range of temperatures: 25, 100, 200, and 300 °C, and five strain rates: 0.001, 0.005, 0.01, 0.05, and 0.1 s⁻¹. The flow curve depicted an inverse sensitivity with test temperature however, very little positive sensitivity was observed for strain rate at higher temperatures. Notably, type-B serrations were noted at temperatures below 100 °C and lower strain rates of 0.01 s⁻¹. To quantify the flow behavior, three distinct prediction models were utilized: artificial neural network (ANN), Johnson–Cook (J–C) and Modified Arrhenius (M–A) model, where ANN model demonstrated notably enhanced prediction accuracy with Average Absolute Relative Error (AARE) of 1.77%, as compared 3.42% and 4.26% for J–C and M–A models, respectively. Furthermore, structure-property correlation was established by conducting electron backscatter diffraction (EBSD) analysis on identical tensile samples subjected to a strain of 17% under varying test conditions. The Kernel Average Misorientation (KAM) was found to be higher (0.84°) at 0.01 s⁻¹ strain rate as compared to 0.001 s⁻¹ (0.74°) confirming the occurrence of dynamic recovery at lower strain rate. However, the maximum average Grain Orientation Spread (GOS) was found to be 3.6° at 300 °C and 0.001 s⁻¹ strain rate confirming the absence of recrystallization at any of the test conditions due to the low strain level.

Keywords Al–Mg alloys · Structure-property correlation · Constitutive modelling · Serrations

1 Introduction

Aluminum is a material of choice for a wide range of industries including automobile, building and construction, ship manufacturing, packaging, and cryogenics because of their lightweight nature, superior corrosion resistance and excellent formability. Among the various aluminum alloys, Al–Mg alloys (AA5XXX) offer an excellent balance of both formability as well as strength. The magnesium content in these alloys typically ranges from approximately 0.5 to 5 wt%, which provides the enhances strength. However, as the magnesium content increases, the secondary β-phase

(Al₃Mg₂) precipitates along grain boundaries through heterogeneous nucleation and growth [1, 2] reducing the formability.

Numerous studies have been conducted on experimental investigations of the flow behavior of Al–Mg alloys using uniaxial tensile and compression tests. For instance, Ozturk et al. [3] conducted a similar study on AA5052-H32 samples, analyzing various strain rates and test temperatures ranging from room temperature to 300 °C, within the strain rate range of 0.0083–0.16 s⁻¹. The effect of temperature on the strain hardening coefficient, strain rate sensitivity, strength coefficient, and total elongation was also examined.

To explain the flow behavior, various constitutive and data-based models have been proposed for various loading conditions over the years [3–7]. Most of these models considers strain rate, temperature, and strain effects. The constitutive model given by Zener et al. [8] and Sellar et al. [9] also considered the effect of strain rate and temperature. Whereas Johnson–Cook (JC) [10] and Zerilli–Armstrong (ZA) [11] models also consider strain in addition making them widely acceptable. However, these models do not

✉ K. Narasimhan
nara@iitb.ac.in

¹ Department of Metallurgical Engineering and Materials Science, Indian Institute of Technology Bombay, Powai, Mumbai 400076, India

² Department of Mechanical Engineering, Indian Institute of Technology Bombay, Powai, Mumbai 400076, India

³ Aditya Birla Science and Technology Company Private Limited, Navi Mumbai 410208, India

account for thermally activated phenomena such as recovery and recrystallization.

Sellar et al. [12] incorporated a strain softening function to consider the effects of thermal activation processes. Over the years, constitutive models specific to applications and materials have been proposed. Guo et al. [13, 14] developed a constitutive model specially for aluminum, utilizing multiple linear functions for flow modeling whereas Lee et al. [15] developed a model to understand the variability in properties due to micro porosity. Another novel constitutive equation was proposed by Guo et al. [16], which combines a linear softening term and peak stress to predict the flow behavior of AA5052 aluminum alloys. Song et al. [17] compared the Johnson–Cook (J–C) constitutive model with the correlation term proposed by Huh and Kang [18]. Arrhenius-type constitutive models have also received significant attention from researchers [19–24]. Jiang et al. [25] and Rezaei et al. [26] have used modified J–C and Arrhenius type constitutive model to predict the compressive flow behavior of aluminum alloys. These models incorporate the effects of strain, strain rate, and temperature to improve prediction accuracy. Back-propagated artificial neural network (BP-ANN) models have demonstrated excellent prediction accuracy for flow behavior [20, 22, 23, 27].

Flow curves are deformation mode dependent. Most of these investigations have primarily centered around phenomenological predictive models, emphasizing the compressive flow behavior of the AA5052 alloy. However, for most of the deep drawing and forming operations, these alloys are subjected to complex tensile stresses at warm forming temperatures of 150–300 °C. Furthermore, a comprehensive endeavor to comprehend the tensile flow behavior of the AA5052 alloy, encompassing its prediction and the establishment of a structured relationship between microstructure and properties at the warm forming temperatures, has been lacking. As a response to this gap, the current study is dedicated to investigating the isothermal tensile behavior of the AA5052 alloy under diverse strain rate and warm temperature conditions. This encompasses the development of both constitutive and data-driven models for enhanced predictive

accuracy. Additionally, the study seeks to establish a correlation between microstructural characteristics and material properties through the utilization of Electron Backscatter Diffraction (EBSD) analysis.

2 Material and Experimental Details

In present study, fully annealed (O-temper) AA5052 alloy sheet of 1 mm thickness was studied. The chemical composition analysis of the AA5052 samples was performed using ICP-OES (inductively coupled plasma optical emission spectrometry), and the weight percentages of the major solute elements are provided in Table 1.

The flow behavior of AA5052 alloy was investigated using isothermal tensile tests conducted along rolling direction. These tests were performed at four different temperatures: 25 °C, 100 °C, 200 °C, and 300 °C and at five strain rates: 0.001–0.1 s⁻¹ at an interval of 0.005 s⁻¹. The tests were conducted on an MTS universal testing machine (UTM). Flat tensile samples were prepared as per ASTM E-8 standard. The tensile sample prepared is illustrated in Fig. 1.

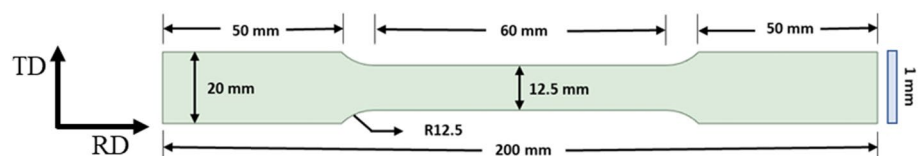
While performing the elevated temperature tests, the specimens were heated using the furnace attached within the Universal Testing Machine (UTM). The heating rate employed was 20 °C/min. To ensure temperature uniformity across the gauge length, the specimen was soaked at the deformation temperature for a duration of 3 min. Following the completion of the tests, the failed samples were air-cooled to room temperature. Figure 2a illustrates the schematic of the elevated tensile test methodology. Additionally, Fig. 2b showcases representative fractured samples.

In order to understand the impact of process parameters on the microstructure, isothermal tensile tests were conducted at 25 °C, 200 °C, and 300 °C, utilizing strain rates of 0.001, 0.01, and 0.1 s⁻¹ until reaching a consistent strain of 17%. Small samples measuring approximately 10 mm in length were extracted from the central gauge region of the tensile specimens. These samples were then subjected

Table 1 Composition analysis of AA5052 test samples in weight percent

	Unit	Mg	Fe	Si	Mn	Cu	Mn	Zn	Cr	Al
Standard	(wt%)	2.2–2.8	<0.4	<0.25	<0.10	<0.10	<0.10	<0.1	0.15–0.35	–
Actual	(wt%)	2.55	0.295	0.067	0.074	0.005	0.074	0.002	0.233	Rest

Fig. 1 Tensile test specimen as per ASTM E-8



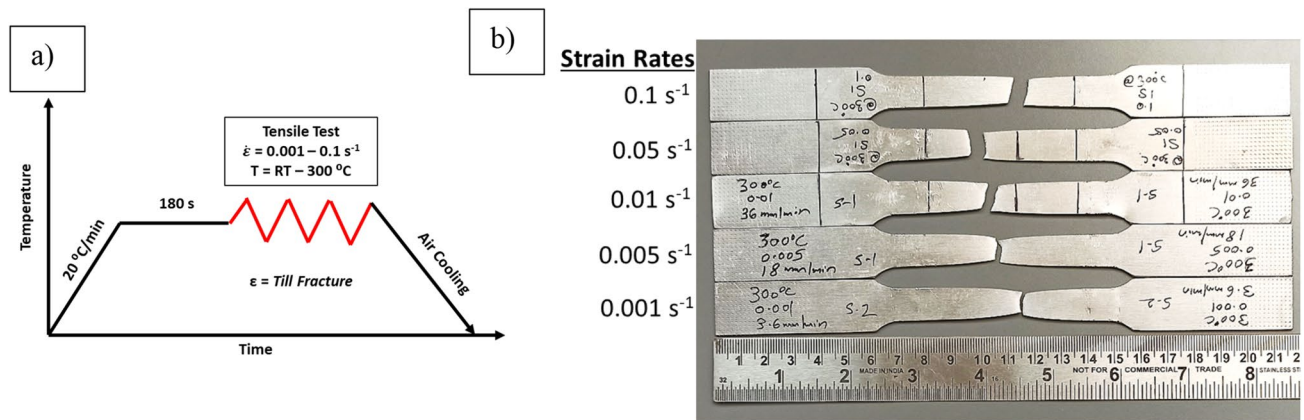


Fig. 2 a Schematic of hot tensile test methodology. b. AA5052 failed samples at 300 °C and different strain rates

to a polishing process in thickness direction to expose the RD-ND (Rolling-Normal Direction) surface.

The polishing procedure involved using emery papers with increasing grit sizes, ranging from 220 to 3000. Subsequently, electropolishing was employed to achieve the mirror finish. The electropolishing procedure entailed immersing the samples in a solution containing 20% vol. perchloric acid and 80% vol. ethanol, while maintaining a temperature below 10 °C. The electropolishing process lasted for 20 s, with a voltage of 20 V and an electrolyte flow rate of 20 ms⁻¹.

EBSM analysis was carried out using an OXFORD fast CCD detector mounted on ZEISS Gemini 300 Field Emission Scanning Electron Microscope (FESEM) on the electropolished samples for different test temperature and strain rate conditions, along with the as-received sample. The scan was conducted on an area of 300 × 300 μm with a step size of 0.2 μm. The EBSM scan data was further analysed using HKL Channel 5 analysis software to understand the grain size distribution and grain misorientation at various test conditions. A detailed discussion and illustration of as-received and deformed microstructure is presented in the microstructural analysis section from Figs. 8, 9, 10, 11 and 12.

3 Isothermal Uniaxial Tensile Tests

The stress and strain data from all the tensile experiments were assimilated. The stress values were plotted against strain values for various temperature and strain rate conditions. To confirm the obtained flow curve at each condition, three repeatability tests were conducted at all test conditions.

3.1 Flow Behavior of AA5052 Alloy

To understand the effect of varying test temperature, stress-strain curves were analysed till failure at constant strain rates. Figure 3a–e shows the effect of various test temperature (25–300 °C) at constant strain rates varying from 0.001 to 0.1 s⁻¹ with an interval of 0.005 s⁻¹. Serrations in flow curves were observed at all strain rates for temperatures ranging from 25 to 200 °C as shown in the insets of Fig. 3.

3.2 Strain Hardening Behavior of AA5052 Alloy

To study the materials' strain hardening behavior, the slope was determined for each data point in the plastic region of the flow curves in Fig. 3 under various test conditions. This slope is the work hardening rate and is denoted as " θ ". θ was then plotted against the strain for different test temperatures at a constant strain rate. Work hardening plots at various strain rates are illustrated in Fig. 4.

4 Constitutive Models

In this study, J–C, modified Arrhenius and backpropagated Artificial Neural Network (BP-ANN) modeling techniques were used to forecast the flow characteristics of AA5052 alloy till Ultimate Tensile Strength (UTS). We subsequently assessed the accuracy of these predictions by comparing them to experimental data using the Average Absolute Relative Error (AARE) and coefficient of determination (R^2).

4.1 Modified Arrhenius Constitutive Model

A constitutive model correlating various parameters of the conducted tensile test with the flow stress was developed. Traditionally, the power law (Eq. 1) and exponential law

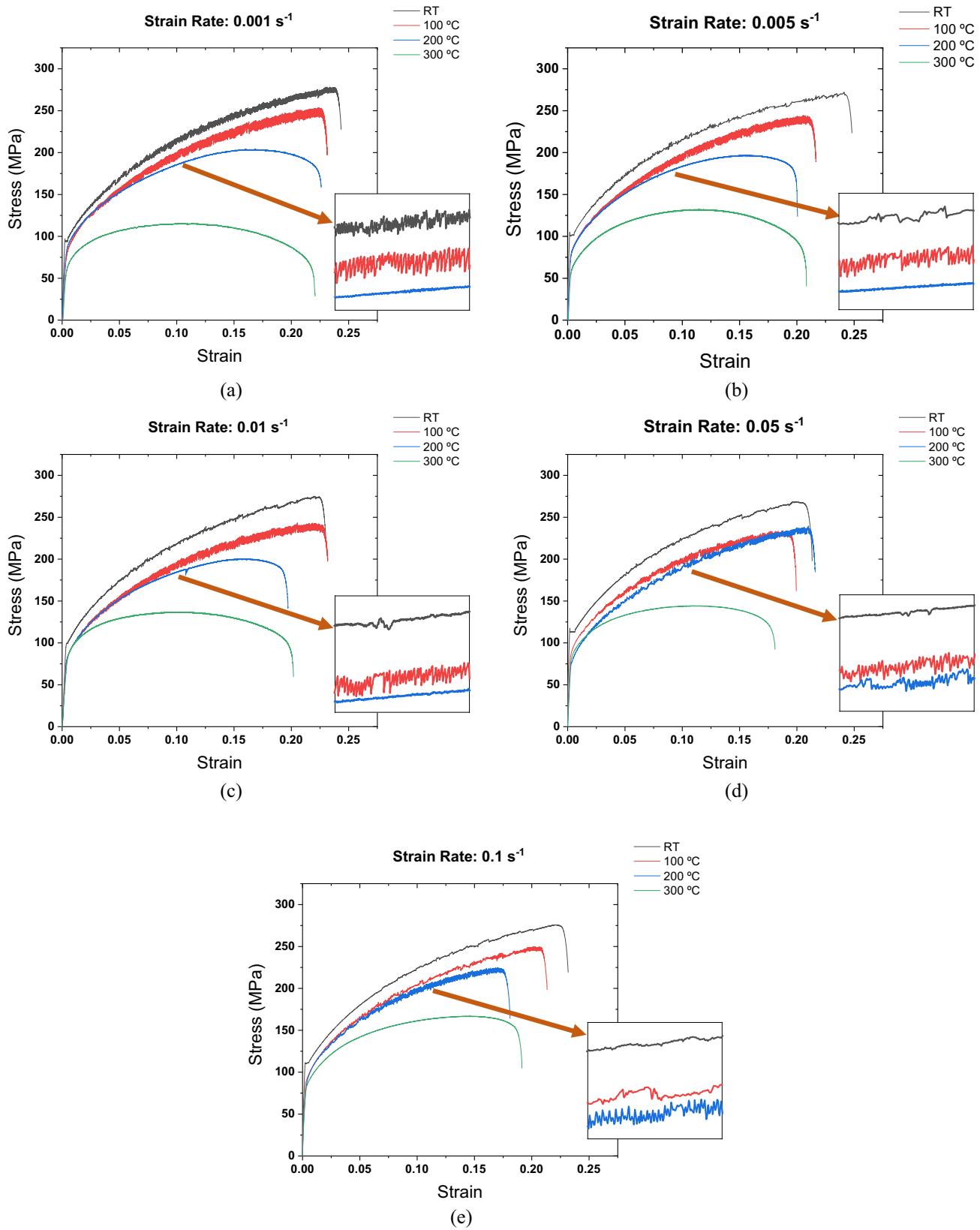


Fig. 3 Isothermal flow curves of AA5052 samples at various strain rates (s⁻¹): **a** 0.001, **b** 0.005, **c** 0.01, **d** 0.05, **e** 0.1

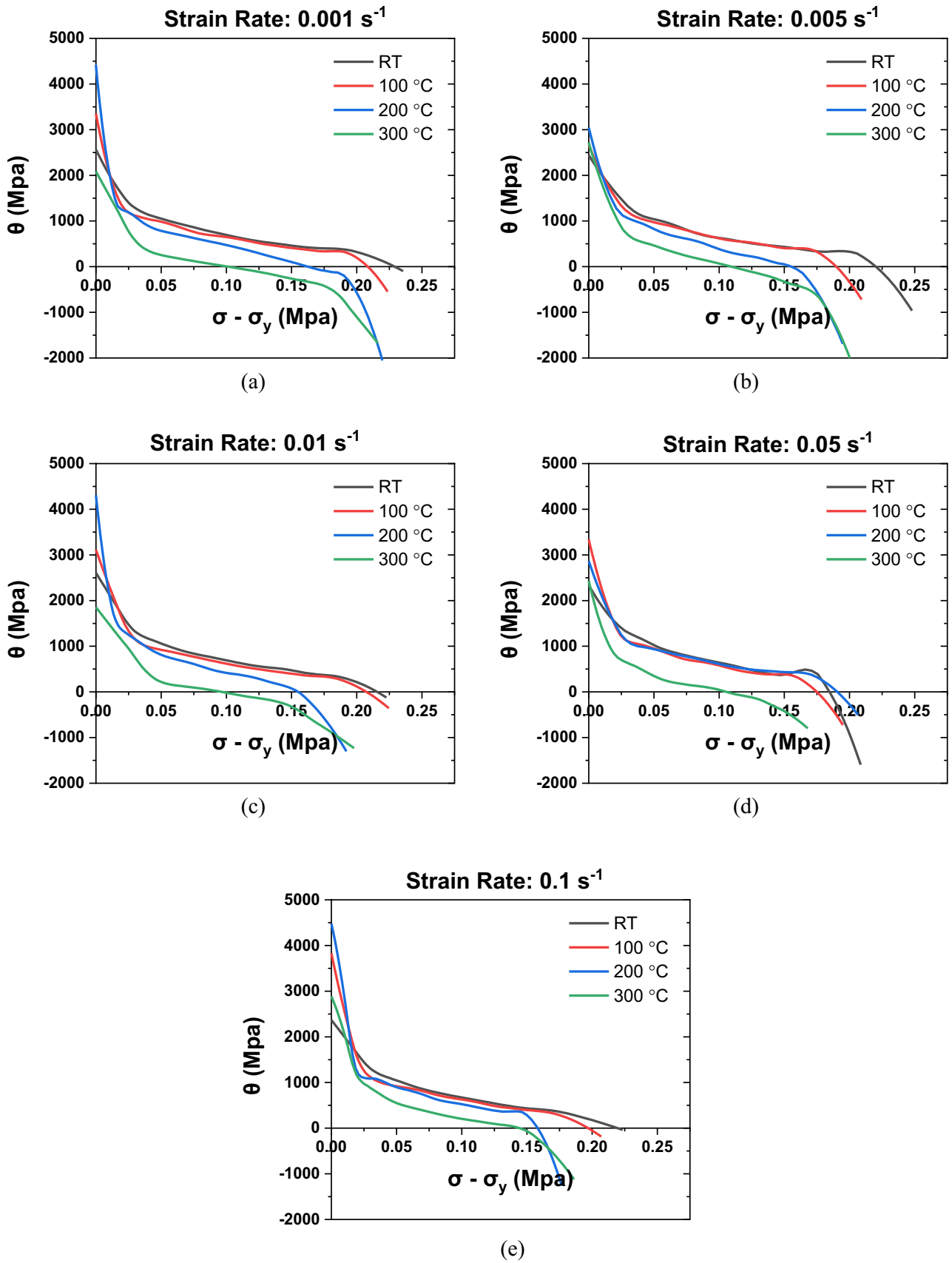


Fig. 4 K-M plot for strain hardening rates vs net flow stress for AA5052 alloy at various strain rates (s^{-1}): a 0.001, b 0.005, c 0.01 d 0.05, e 0.1

(Eq. 2) have been employed to establish constitutive relations during specific processing [28].

$$A_1 \sigma^{n_1} \cdot \exp\left(-\frac{Q}{RT}\right) \tag{1}$$

$$\dot{\epsilon} = A_2 \cdot \exp(\beta\sigma) \cdot \exp\left(-\frac{Q}{RT}\right) \tag{2}$$

Both these laws have limited validity for the actual day to day thermo mechanical processes like rolling, extrusion etc. due to their wide range of temperature and strain rates. To address these limitations, a unified function called the Hyperbolic Sine law was employed. This function combines the equations from both laws [29, 30] and is presented as Eq. (3) below.

$$\dot{\epsilon} = A[\sinh(\alpha\sigma)]^n \cdot \exp\left(-\frac{Q}{RT}\right) \tag{3}$$

In the equation, constants A , β , n_1 , α , and n are adjustable parameters. Q represents the hot deformation activation energy. The value of α is determined by the ratio of β to n_1 . When $\alpha\sigma$ is less than 0.8, the hyperbolic sine law simplifies to a power law, whereas when $\alpha\sigma$ exceeds 1.2, it transforms into an exponential law.

4.1.1 Constitutive Parameters' Calculation

The parameter β was evaluated by a fitting $\ln \dot{\epsilon}$ and σ for various test temperature using Eq. (4), as illustrated in Fig. 5a. The parameter n_1 was estimated by linearly fitting $\ln \dot{\epsilon}$ and $\ln \sigma$, employing Eq. (5), as depicted in Fig. 5b. The stress multiplier (α) is calculated by taking the ration of β and n_1 . For all the parameters the average values were considered.

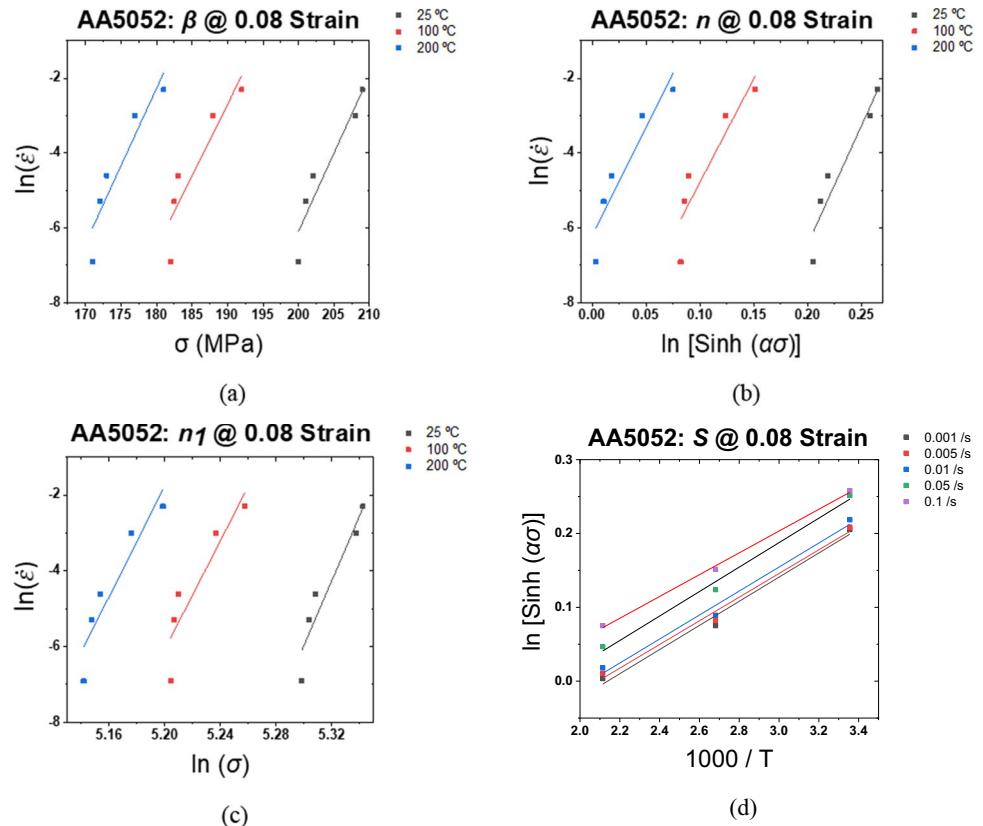
$$\ln \dot{\epsilon} = \ln A_1 + n_1 \ln \sigma - \frac{Q}{RT} \tag{4}$$

$$\ln \dot{\epsilon} = \ln A_2 + \beta \sigma - \frac{Q}{RT} \tag{5}$$

For a constant temperature, linear fitting of $\ln \dot{\epsilon}$ and $\ln[\sinh(\alpha\sigma)]$ was utilized to estimate n using Eq. (6), as depicted in Fig. 5c. Likewise, at a constant strain rate $\dot{\epsilon}$, linear fitting of $\ln[\sinh(\alpha\sigma)]$ and $1/T$ was used to estimate the parameter S , as shown in Fig. 5d. This value of S can be utilized to determine the activation energy Q using Eq. (7).

$$\ln \dot{\epsilon} = \ln A + n \ln[\sinh(\alpha\sigma)] - \frac{Q}{RT} \tag{6}$$

Fig. 5 Linear plot: **a** $\ln(\dot{\epsilon})$ versus peak stress, **b** $\ln(\dot{\epsilon})$ versus $\ln(\sigma)$, **c** $\ln(\dot{\epsilon})$ versus $\ln[\sinh(\alpha\sigma)]$ at various temperatures and **d** $\ln[\sinh(\alpha\sigma)]$ versus $1000/T$ for various strain rates to material constants of Arrhenius model at $\epsilon=0.08$ for AA5052



$$Q = R \left[\frac{\partial \ln \dot{\epsilon}}{\partial \ln [\sinh(\alpha\sigma)]} \right]_T \times \left[\frac{\partial \ln [\sinh(\alpha\sigma)]}{\partial \left(\frac{1}{T} \right)} \right] = RnS \quad (7)$$

The hyperbolic sine equation can be reformulated using the Zener Holloman parameters (Z), which captures the synergic effect of temperature and strain rate [6, 31]. To calculate the values of Z , Eq. (8) is utilized. Subsequently, constants A and n is estimated by linearly fitting $\ln(Z)$ and $\ln[\sinh(\alpha\sigma)]$.

$$\ln Z = \ln A + n \ln [\sinh(\alpha\sigma)] \quad (8)$$

In order to consider the influence of strain, the aforementioned parameters are now determined for different strain values [21]. In this study, strain values ranging from 0.04 to 0.16 were utilized, with an interval of 0.02, for calculating the parameters. In the subsequent section, a representative calculation of the constitutive parameters is presented specifically for a strain value of 0.08.

The constitutive equations for AA5052 alloy at a strain value of 0.08 can be represented as Eq. (9).

$$\dot{\epsilon} = 4079 \times [\sinh(0.0038\sigma)]^{4.36} \times \exp \left[\frac{55 \times 10^3}{RT} \right] \quad (9)$$

The effect of various constants such as Q , n , α , and $\ln A$ in the constitutive model has been investigated, with respect to varying strain [8, 32–35]. Various parameters calculated at multiple strain for AA5052 alloy were plotted. It was observed that an order 5 polynomial provided the best fit. The polynomial equations obtained through the polynomial fitting, including all the parameters, are shown in Eq. 10–13. The activation energy was found to be ranging from 38.5 to 58.7 kJ/mol for strain ranging between 0.04 and 0.16.

$$\alpha = 796.04\epsilon^5 - 385.11\epsilon^4 + 69.809\epsilon^3 - 5.7108\epsilon^2 + 0.1786\epsilon + 0.0048 \quad (10)$$

$$n = 4E + 07\epsilon^5 - 2E + 07\epsilon^4 + 3E + 06\epsilon^3 - 198793\epsilon^2 + 7602.9\epsilon - 78.331 \quad (11)$$

$$Q = 6E + 10\epsilon^5 - 3E + 10\epsilon^4 + 5E + 09\epsilon^3 - 4E + 08\epsilon^2 + 1E + 07\epsilon - 176284 \quad (12)$$

$$\ln(A) = 9E + 06\epsilon^5 - 4E + 06\epsilon^4 + 562892\epsilon^3 - 39710\epsilon^2 + 1390.1\epsilon - 14.984 \quad (13)$$

4.2 Johnson Cook Constitutive Model

The Johnson–Cook (JC) model is widely accepted in the field of constitutive modeling because of its simplicity and small number of constants [36]. However, JC model's

predictions are not accurate for higher strain rates conditions as it does not consider any microstructural effect [19]. The JC model can be expressed as follows [37]:

$$\bar{\sigma} = (A + B\bar{\epsilon}^n) \left[1 + C \ln \left(\frac{\dot{\bar{\epsilon}}}{\dot{\bar{\epsilon}}_{Ref.}} \right) \right] \left[1 - \left(\frac{T - T_{Ref.}}{T_m - T_{Ref.}} \right)^m \right] \quad (14)$$

where $\bar{\sigma}$ and $\bar{\epsilon}$ represents flow stress and plastic strain, respectively. B represents strain hardening coefficient, n represents exponent of strain hardening, C represents the strain rate hardening coefficient, m represents softening coefficient caused by thermal softening. A represents the yield stress value for reference condition. The three terms in Eq. (14) represents the strain hardening, strain rate and thermal softening effects, respectively. However, in the original model all the three effects were considered separately.

4.2.1 Johnson–Cook Parameters' Calculation

Various parameters of JC model were estimated by selecting reference temperature and strain rates among various test conditions and utilizing the obtained flow curves through various tensile tests conducted.

4.2.1.1 Reference Strain Rate and Temperature Condition In this study, 100 °C and 0.001 s⁻¹ were selected as the reference temperature and strain rate, respectively. At these reference conditions, the second and third term of Eq. (14) becomes one and it takes the form

$$\bar{\sigma} = (A + B\bar{\epsilon}^n) \quad (15)$$

where the parameter n and B can be estimated by fitting the plastic region of flow curves to (15) whereas the yield stress was taken as constant A .

4.2.1.2 Fixed Strain Rate and Reference Temperature Condition For a fixed strain rate and reference temperature, the third term of Eq. (14) equals to one and it simplifies to the following equation:

$$\bar{\sigma} = (A + B\bar{\epsilon}^n) \left[1 + C \ln \left(\frac{\dot{\bar{\epsilon}}}{\dot{\epsilon}_{Ref.}} \right) \right] \quad (16)$$

The parameter *C* was calculated by drawing a plot of $\ln(1 - (\bar{\sigma}/(A + B\bar{\epsilon}^n)))$ against $\ln(\frac{\dot{\bar{\epsilon}}}{\dot{\epsilon}_{Ref.}})$ and calculating the slope. Another approach to taking an average value of *C* corresponding to multiple strains.

4.2.1.3 Fixed Temperature and Reference Strain Rate Condition In case of fixed temperature and reference strain rate, the second term of Eq. (14) equals to one and it simplifies to the following Eq:

$$\bar{\sigma} = (A + B\bar{\epsilon}^n) \left[1 - \left(\frac{T - T_{Ref.}}{T_m - T_{Ref.}} \right)^m \right] \quad (17)$$

The parameter, ‘*m*’ was estimated by drawing a plot between $\ln(1 - (\bar{\sigma}/(A + B\bar{\epsilon}^n)))$ versus $\ln(\frac{T - T_{Ref.}}{T_m - T_{Ref.}})$ and calculating the slope. Alternatively, it can also be taken as the average value for multiple strain levels. Table 2 presents the calculated JC material constants for AA5052 alloy.

$$\bar{\sigma} = (104 + 459\bar{\epsilon}^{-0.53}) \left[1 + 0.016 \ln \left(\frac{\dot{\bar{\epsilon}}}{0.001} \right) \right] \left[1 - \left(\frac{T - 298}{922 - 298} \right)^{1.22} \right] \quad (18)$$

4.3 Back Propagated ANN Model

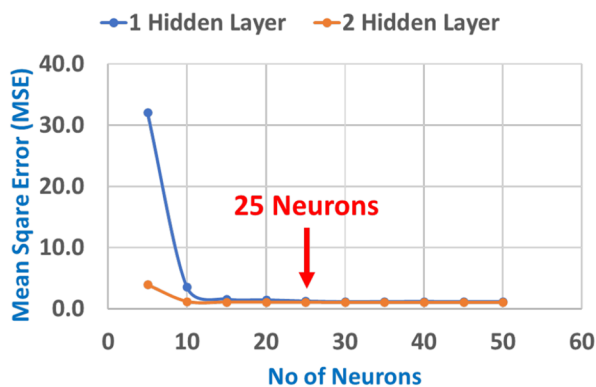
Flow behavior of a material exhibit complex behavior, which is affected by numerous factors such as strain, strain rate, temperature, and others. Consequently, accurately describing the flow curve using regression methods alone becomes challenging [38]. To overcome this challenge, an artificial neural network (ANN) model with backpropagation was developed using MATLAB R2020b.

This model aims to analyze the flow behavior of Al–Mg alloys by considering strain, temperature and strain rate as input variables, whereas true stress was considered as the output parameter. To evaluate the model's performance, the entire dataset was split into 95% and 5% as training and testing set, respectively. The training dataset with 81,617 data points was used across the aforementioned variables.

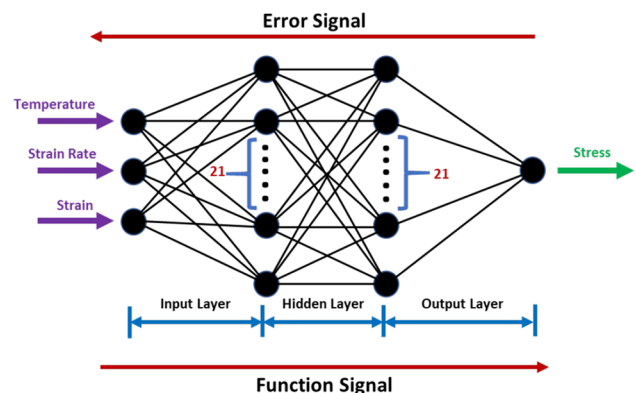
To determine the optimal number of hidden layer neurons, the mean square error (MSE) given by Eq. (11) was utilized as a metric. The MSE is calculated by comparing the experimental values (*E_i*) with the predicted values (*P_i*). By analyzing the results shown in Fig. 6a, the minimum MSE was found for a network structure consisting of 25 neurons distributed across 2 hidden layers. The model architecture is depicted in Fig. 6b.

Table 2 JC material constants estimated for AA5052 alloy

A	B	<i>n</i>	C	<i>m</i>	T _{Ref.} (°C)	ε _{Ref.}
104	459	0.53	0.016	1.22	100	0.001



(a)



(b)

Fig. 6 a Trend of MSE with hidden layer and number of neurons for AA5052. b Final architecture of ANN model for minimum MSE

$$MSE = \frac{1}{N} \sum (E_i - P_i)^2 \quad (19)$$

Normalization of the input and output variables is crucial for improving the convergence speed and prediction accuracy of a BP-ANN model, especially when the numerical values of these variables are distributed in distinct ranges and dimensions. To achieve dimensionless variables with approximately the same magnitude, a normalization process is applied to the initial true stress–strain data. Li et al. [22] have shown that using coefficients of 0.05 and 0.25 in Eq. (20) as regulating parameters effectively narrows the magnitude of the normalized data within the range of 0 to 0.3. This specific magnitude range has been determined through a trial-and-error approach and has been found to enhance the convergence speed and prediction accuracy of the model.

$$x_n = 0.05 + 0.25 \times \frac{x - 0.95x_{min}}{1.05x_{min} - 0.95x_{min}} \quad (20)$$

In the equation, x_{max} and x_{min} represent the maximum and minimum values of variables, respectively. The variable x_n represents the normalized value, which is obtained by scaling the original values within the range of 0 to 0.3 using the maximum and minimum values.

For the current neural network, the activation functions Tansig and Purelin were selected for the hidden and output layers, respectively. The training function Trainbr and learning function Learngd were chosen for the training process. To ensure stability and convergence, a slower rate of learning (0.000) was used. The regression values (R -values) obtained for AA5052, using a network with 2 hidden layers and 25 neurons, were found to be 0.9998 for training, validation, testing and overall stages, as depicted in Fig. 7. The high regression values ensure the better predictability of the ANN model. The prediction accuracy for various models has been presented in the results section.

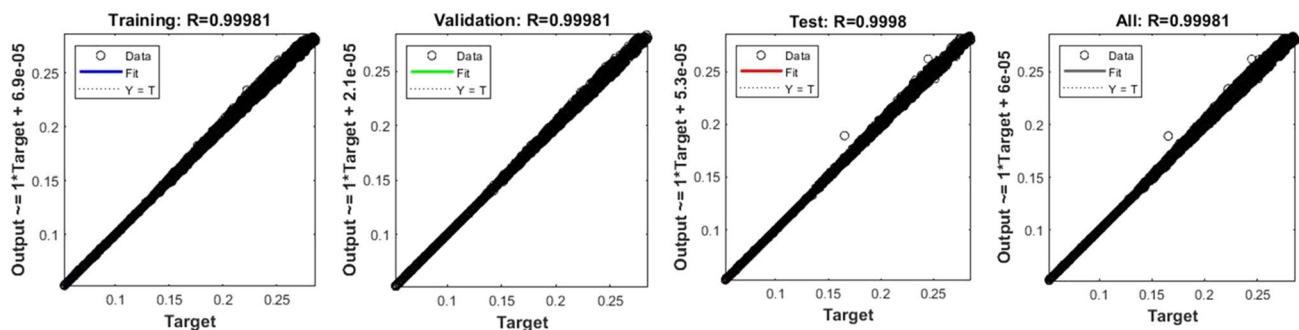


Fig. 7 R-value for the final ANN model of AA5052 alloy

5 Microstructural Analysis

To develop a correlation between the obtained flow behavior of AA5052 alloy with microstructural evolution, EBSD analysis was conducted for identical strain tensile samples. The minimum failure strain obtained during the conducted tensile experiments for all test temperatures (25–300 °C) and strain rates (0.001–0.1 s⁻¹) was found to be 18%. Therefore, to study the microstructural evolution, additional tensile tests at constant strain of 17% was conducted at 25 °C, 200 °C and 300 °C temperature and 0.001, 0.01 and 0.1 s⁻¹ strain rates.

5.1 As-Received Microstructure

The microstructural analysis of the as-received sheet was conducted to establish the baseline. The colored Inverse Pole Figure (IPF) map, image quality (IQ) map, Kernel Angle Misorientation (KAM), Grain Orientation Spread (GOS) and pole figures for bulk texture has been presented in Fig. 8. An average grain size of $22.9 \pm 1.9 \mu\text{m}$ and low angle grain boundary (LAGB) fraction of 0.48 was observed in the as-received sample. The KAM graph presented in Fig. 8c was estimated considering third nearest neighbor and maximum misorientation of 3°. The average KAM and GOS valued was found to be 0.57° and 0.49° for as-received material. The texture components were estimated by analysis of EBSD data as well as the bulk texture measurement using XRD technique on a Malvern Panalytical Empyrean machine. The pole figures and Orientation Distribution Function (ODF) maps drawn from both the methods were found to be matching. The pole figures from bulk texture analysis for (111), (200), (220) and (311) has been illustrated in Fig. 8e with brass and Cube texture as the major components.

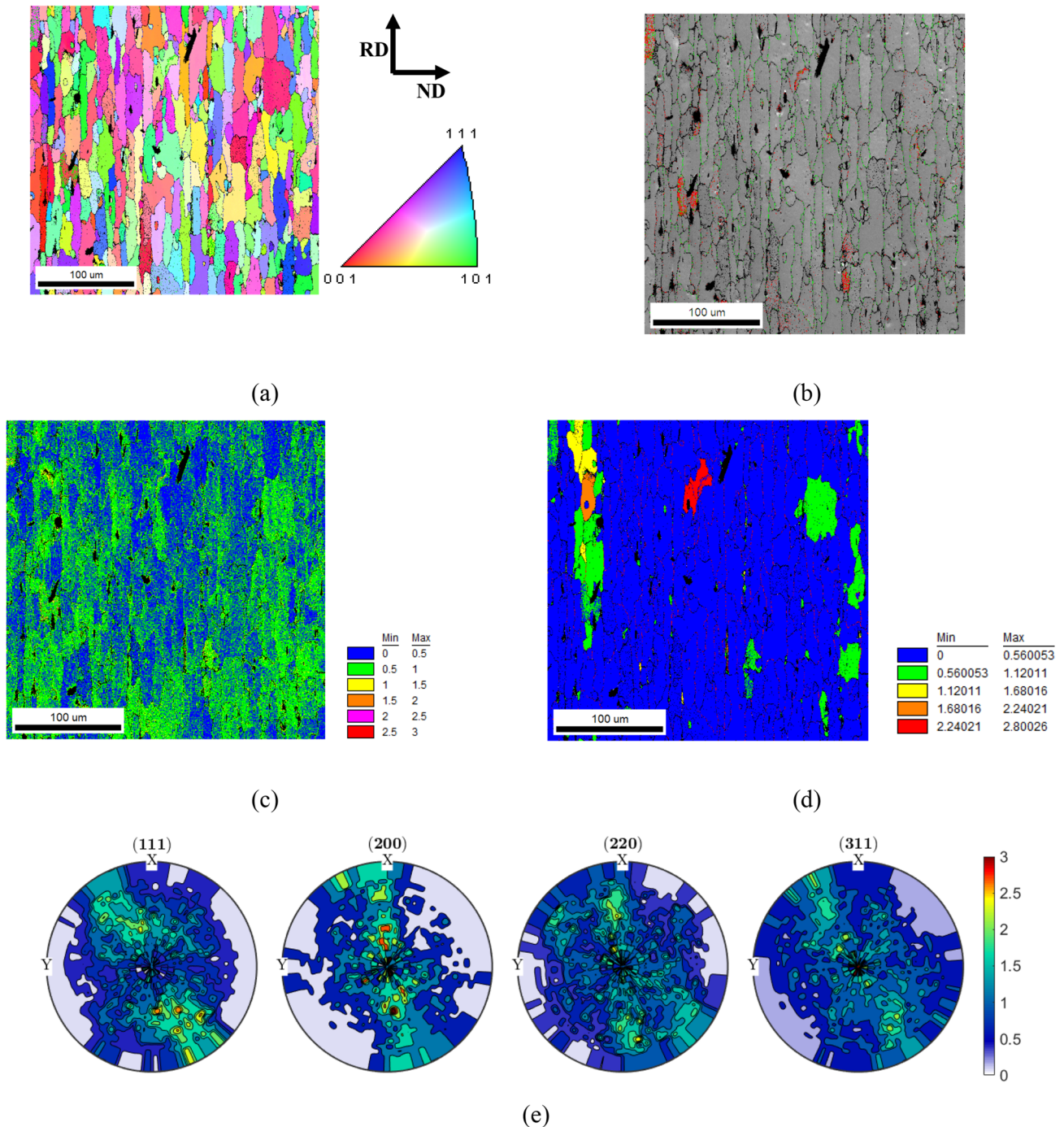


Fig. 8 As-received microstructure in terms of **a** IPF map, **b** IQ map, **c** KAM, **d** GOS, **e**Texture Pole figures

5.2 Deformed Microstructure

5.2.1 EBSD Analysis

To study the evolution of microstructure with varying temperature and strain rates, EBSD scans were conducted at all test temperatures. The scan was performed for all the 9 test condition samples along with as-received sample on

an area of $300 \times 300 \mu\text{m}$ with a step size of $0.2 \mu\text{m}$. Inverse Pole Figure (IPF) maps for all temperature and strain rate conditions are illustrated in Fig. 9.

The IPF maps represent the orientation of a chosen axis of specimen (in this case ND) in the local reference frame of each grain. With no specific orientation to any of the $\langle 111 \rangle$, $\langle 001 \rangle$ and $\langle 101 \rangle$ direction in the IPF maps, it was clearly evident from Fig. 9 that there is no

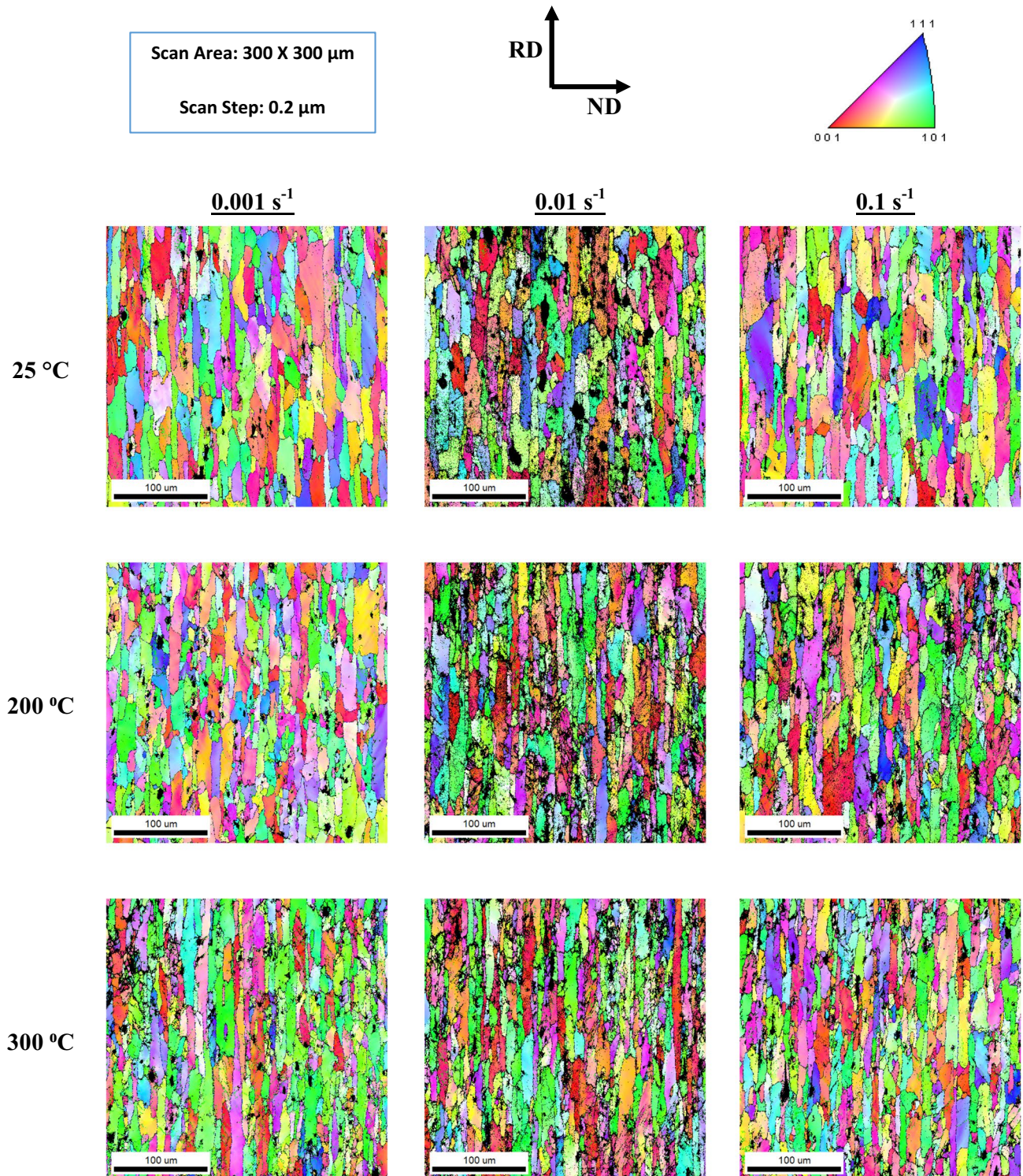


Fig. 9 Inverse pole figures of AA5052 alloy with varying temperature of 25–300 °C (Top–Bottom) and varying strain rate 0.001–0.1 s⁻¹ (Left–Right)

significant texture at any of the test conditions and all the grains are randomly oriented. However, when moving from right to left in Fig. 9, a darker heterogeneity due to

higher dislocation density was observed at 0.01 s⁻¹ strain rate (central column) as compared to 0.1 s⁻¹ strain rate (right column) signifying higher subgrain fraction which

further decreased at lower strain rates of 0.001 s^{-1} (left column).

5.2.2 Grain Size and Grain Boundary Analysis

The EBSD scan data was analysed using HKL Channel 5 analysis software. The grain size distribution, low ($2^\circ\text{--}15^\circ$) and high ($15^\circ\text{--}65^\circ$) angle grain boundary fractions was analysed for varying test conditions. The average grain size and the ratio of Low Angle Grain Boundary (LAGB) and High Angle Grain Boundary (GB) for various strain rates and test temperatures has been listed in Table 3.

The variation of grain size and the ratio of LAGB with Total Grain Boundary (GB) with increasing test temperatures at different strain rates has been presented in Fig. 10a,

b, respectively. An overall decreasing trend of grain size was observed with increasing test temperature whereas the highest average KAM values were observed at the strain rate of 0.01 s^{-1} .

5.2.3 Misorientation Angle Analysis

The misorientation angle distribution was estimated at various temperature and strain rate conditions. The trend of average KAM and GOS values for increasing test temperatures at different strain rates has been presented in Fig. 11a, b, respectively. The highest average KAM value was observed at the strain rate of 0.01 s^{-1} whereas the

Table 3 Average grain size, LAGB and HAGB at various strain rates and test temperatures

Strain rate (s^{-1})	Average grain size (μm)			LAGB ($2^\circ\text{--}15^\circ$)			HAGB ($15^\circ\text{--}65^\circ$)		
	25 °C	200 °C	300 °C	25 °C	200 °C	300 °C	25 °C	200 °C	300 °C
0.001	25.2	21.0	19.2	4.1	5.8	4.2	3.0	0.6	1.8
0.01	20.2	19.9	19.1	4.0	5.8	6.5	3.6	0.6	1.0
0.1	26.3	22.1	19.3	8.3	6.6	5.9	3.0	1.1	1.9

Fig. 10 a Grain size distribution and b Kernel Angle Misorientation (KAM) distribution of AA5052 alloy with varying strain rate (s^{-1}) viz. 0.1, 0.01 and 0.001

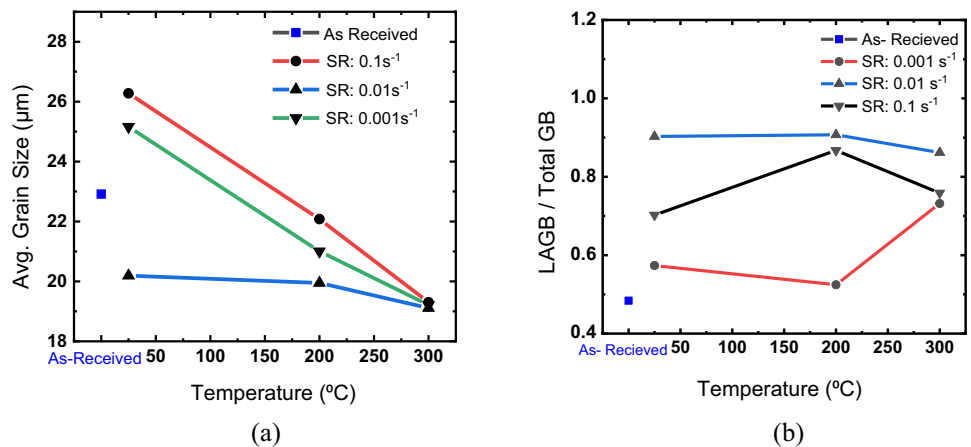
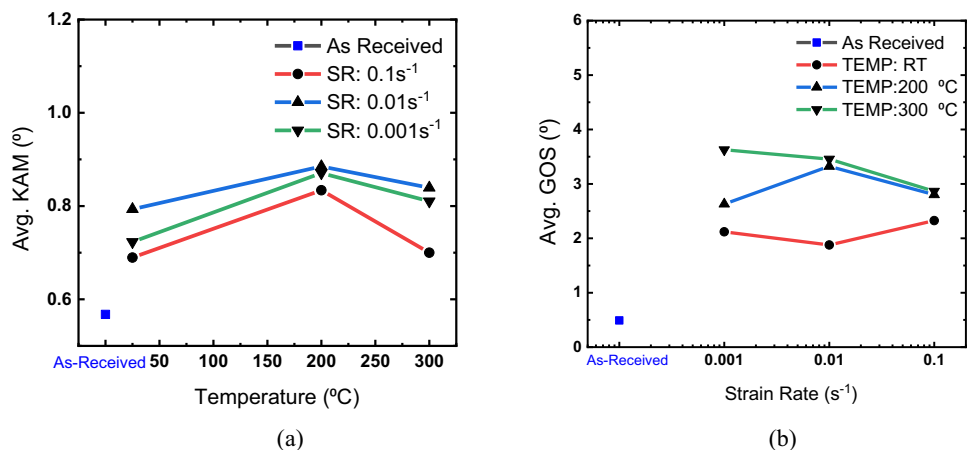


Fig. 11 Misorientation angle distribution trends: a Avg. KAM, b Avg. GOS



average GOS value shows an increasing trend with increasing temperature.

5.2.4 Bulk Texture Analysis

To understand the change in various components of microstructural texture, the scanned data for as-received and deformed samples at 25 °C and 300 °C temperature and 0.1 s⁻¹ strain rate were analysed using MTEX™ open software. The change comparative chart has been presented in Fig. 12 in the form of a radar chart. A very small increase in brass and Cube texture and reduction in Goss texture component was observed in deformed samples as compared to the as-received samples. However, the overall texture intensity of both undeformed and deformed samples was observed to be very low.

6 Results and Discussions

The important observations and results regarding the flow behavior, their predictions and microstructural evolution have been discussed in the following sections.

6.1 Flow Behavior of AA5052 Alloy

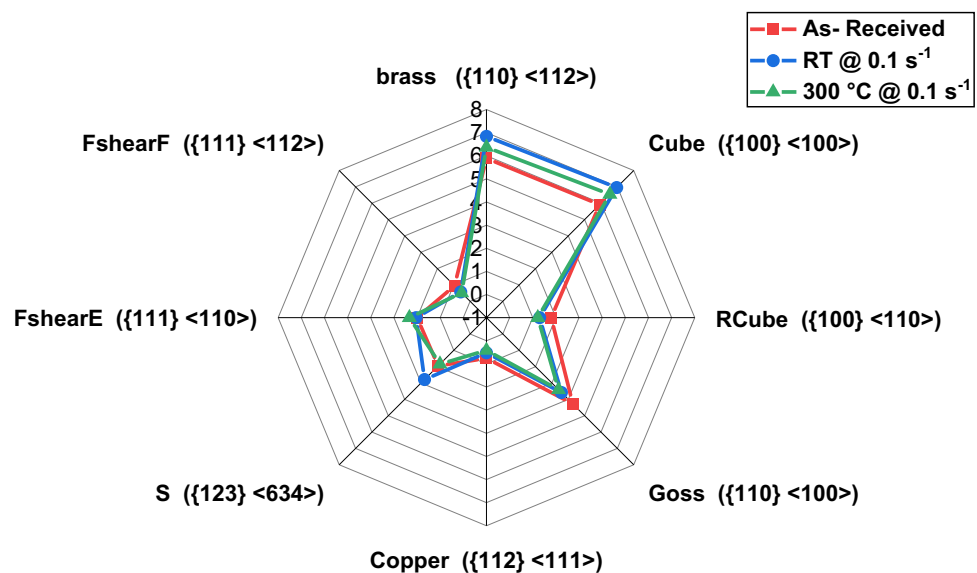
The trend of the flow curves and uniform plastic strain displays a decline as the test temperature rises from 25 to 300 °C, as demonstrated in Fig. 3. A comparable decrease in flow rates was also noted by Prakash et al. [38] when examining the AA5052-H32 material under isothermal tensile tests. This pattern can be ascribed to the phenomenon of thermally activated softening [39]. Moreover, it is evident that the flow curves exhibit minimal sensitivity to strain rate

variation at 25 to 200 °C, indicating a negligible impact of strain rate. However, at 300 °C, a positive strain rate sensitivity effect becomes apparent, as the flow curves exhibit an upward trend with increasing strain rates ranging from 0.001 to 0.1 s⁻¹.

Serrations of Type-B [40] were noted at lower temperatures, specifically within the range of 25 to 200 °C, across all strain rates spanning from 0.001 to 0.1 s⁻¹. These observed serrations are due to well-known Portevin-Le Chatelier (PLC) effect which has been observed for several Al–Mg alloys over a wide range of strain rate and temperatures [41–48]. PLC effect is often regarded as a specific instance of a broader concept known as Dynamic Strain Ageing (DSA) [47]. DSA occurs due to the interaction between solute atoms and dislocations, causing their continuous pinning and unpinning. Over specific strain rate and temperature range, unpinning of several dislocations simultaneously leads to the localization of plastic deformation. On macroscopic level, slip bands form at an approximate angle of 55° to the direction of the applied strain. The propagation of these slip bands along the gauge length of, even at lower stresses than typically required for their initiation, results in the distinctive serrations seen in stress–strain curves. Notably, the insets in Fig. 3 distinctly reveal that the magnitude of serrations in the flow curves is more pronounced for the 25–100 °C range at lower strain rates, while at 200 °C, the magnitude of serrations becomes more significant at higher strain rates.

The relationship between the strain hardening rate (θ) and net flow stress ($\sigma - \sigma_y$), depicted in Fig. 4 following the Kocks–Mecking (K–M) model, provides insight into the tensile work hardening characteristics of the AA5052 alloy. The strain hardening behavior of AA5052 alloy reveals distinct stages: stage III marked by parabolic hardening, followed

Fig. 12 Trend of various texture components with increase in temperature from 25 to 300 °C at strain rate of 0.1 s⁻¹



by stage IV characterized by linear hardening, and finally transitioning into stage V with parabolic transition. The stable hardening exhibited in stage IV was evident primarily at lower temperatures, specifically at 25–200 °C. However, at the elevated temperature of 300 °C, the presence of stage IV was absent. Notably, the curves demonstrate a positive correlation with test temperature, as they shift towards lower values with increasing temperature. The most significant softening was observed at 300 °C illustrating the presence of dynamic recovery. Furthermore, a consistent reduction in the extent of region IV was observed as the test temperature increases. Eventually, the strain hardening process concludes at stage V. The nearly parabolic nature of the transition stage for the AA5052 alloy's test temperature suggests a confluence of slip dislocation bands, dislocation tangling, and dislocation splitting attributed to the interaction of precipitates within the alloy [49].

6.2 Constitutive Modelling and Prediction Accuracy

The alignment between experimental and model-predicted values was assessed by plotting them together. Figure 13 illustrates the comparison between these sets of values, originating from the BP-ANN, J–C, and modified Arrhenius models. To numerically gauge the precision of predictions, the Average Absolute Relative Error (AARE) values were computed for each of these modeling approaches, employing Eq. (21). For AA5052, the resulting AARE values were calculated as 1.77% for BP-ANN, 3.42% for J–C, and 4.26% for the Modified Arrhenius model. This analysis clearly underscores the substantial superiority of prediction accuracy demonstrated by the BP-ANN model, followed by the J–C Model, in comparison to the Modified Arrhenius model.

The diminished precision of the Arrhenius model can be attributed to its utilization of an averaging methodology for estimating constitutive parameters. This approach, despite the high temperature sensitivity exhibited by Al–Mg alloys, contributes to the poorer accuracy observed in this particular model.

$$AARE = \frac{1}{N} \sum_{i=1}^{i=N} \left| \frac{\sigma_x^i - \sigma_y^i}{\sigma_x^i} \right| \times 100 \quad (21)$$

For assessing the degree of agreement between actual and forecasted stress values, the coefficient of determination (R^2 value) was computed across all three prediction models: BP-ANN, J–C, and Modified Arrhenius. This analysis is presented in Fig. 14. The notably enhanced predictive capability of the BP-ANN model was unmistakably apparent, as reflected in its coefficient of determination values: 0.9973 for BP-ANN, 0.9623 for J–C, and 0.9483 for the Modified Arrhenius models. This signifies a remarkable performance

in prediction accuracy by the BP-ANN model. These outcomes align with those documented by various researchers [[21–23, 27] further corroborating the superior predictive capacity of the BP-ANN model.

6.3 Structure-Property Correlation

The inverse pole figures depicted in Fig. 9 illustrate the characteristics of AA5052 alloy across varying temperatures and strain rates. The findings reveal a uniform growth of grains lacking any discernible texture development or recrystallization as confirmed by the texture trend presented in Fig. 12 and absence of sudden softening stage representing recrystallization phenomenon [50] in KM plots illustrated in Fig. 4. This outcome is attributed to the limited strain applied, reaching a maximum of only 17%, as there has been several reported instances of recrystallization and texture evolution for aluminum alloys subjected to higher strain (> 30%) [51–60]. Notably, the alloy's initial state of complete annealing eliminated the presence of any pre-existing strain effects.

Observations of grain size trends demonstrate a small reduction as temperature rises. Specifically, the average grain size diminishes from 22.9 μm in the as-received sample to approximately 19.3 μm in samples subjected to 300 °C across all strain rates, as depicted in Fig. 10a. The fraction of subgrain was also observed to be increasing with decreasing strain rate (central column in Fig. 9) signified by increased darker heterogeneity inside the grains [61]. However, the fraction of sub grains experiences a decrease upon further reduction in strain rate (left column in Fig. 9). This reduction can be attributed to dynamic recovery (DRV). During DRV the opposite dislocations annihilate, and the remaining dislocations rearrange to form subgrain boundaries making the inside of the grain clearer [62, 63]. This shift is visually evident in the clearer inverse pole figures present in the left column, linked to the slowest strain rate of 0.001 s^{-1} , when compared to the central column portraying a strain rate of 0.01 s^{-1} in Fig. 9. The proposed DRV was also confirmed by average KAM trend presented in Fig. 11a, which shows highest values for the strain rate of 0.01 s^{-1} . The presence of DRV at higher temperature and lower strain rate can be attributed to the observed inverse sensitivity of the flow curves with test temperature. The absence of stage IV hardening phase in the hardening plots at higher test temperature can also be explained due to the presence of dynamic recovery causing the softening to be higher as compared to the strain hardening.

It is worth noting that despite these observations, no instances of recrystallization were noted at any of the tested temperatures and strain rates. Several researchers have considered average GOS values below a critical value (usually 2°–3° for aluminum alloys) to identify the recrystallized

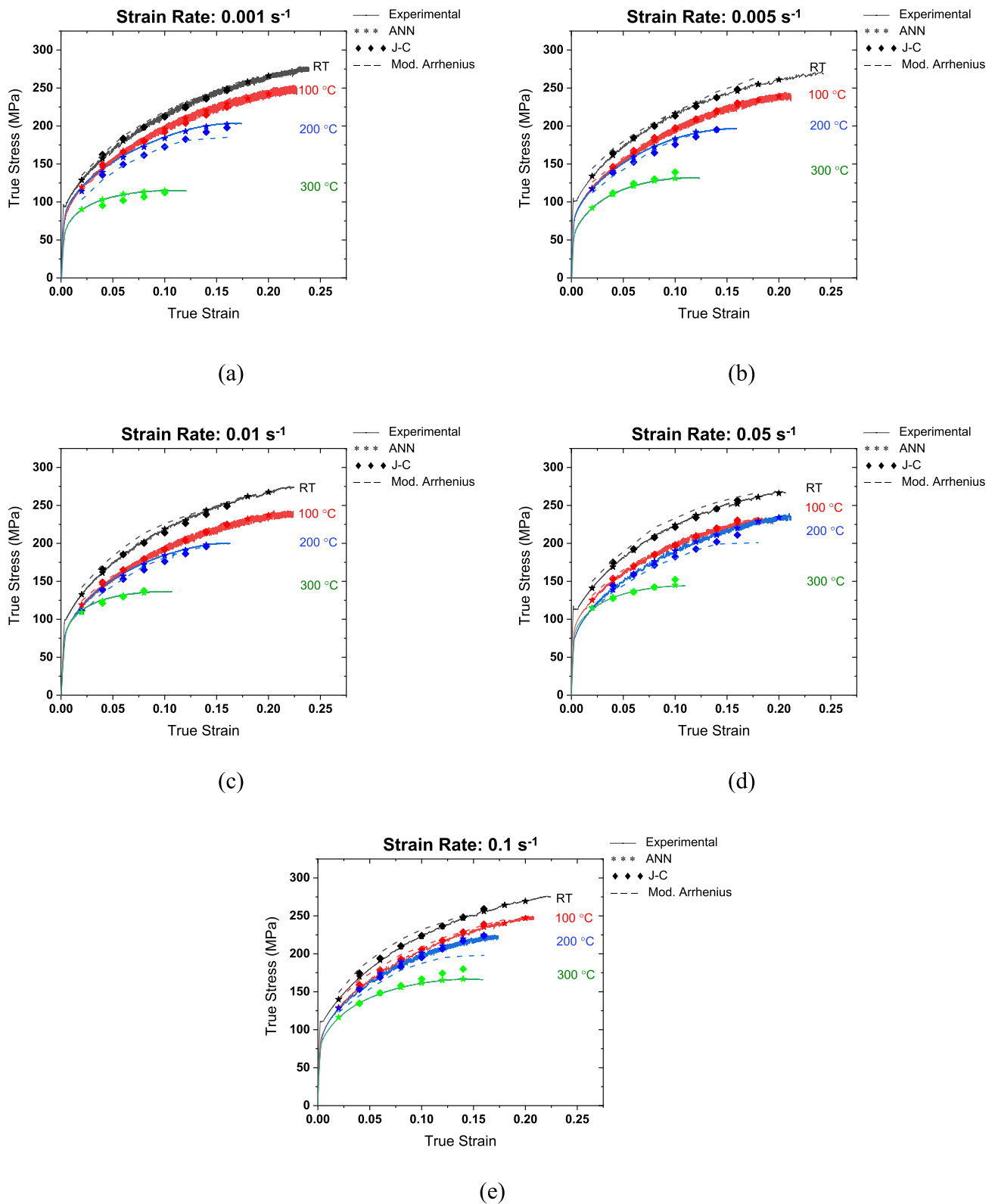


Fig. 13 Flow behavior comparison of AA5052 wrt. experimental, ANN, J-C and Mod. Arrhenius model predictions at strain rates(s^{-1}): **a** 0.001, **b** 0.005, **c** 0.01, **d** 0.05, **e** 0.1

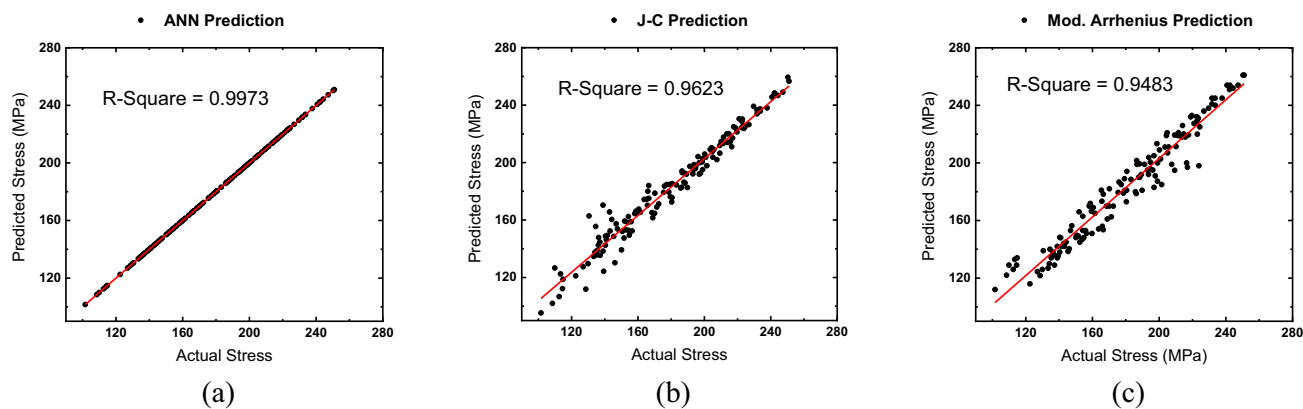


Fig. 14 Coefficient of determination showing the goodness of fit for stress prediction by **a** BP-ANN, **b** J–C and **c** Modified Arrhenius Model

and deformed grains in a microstructure [64, 65]. However, the increasing trend of GOS with temperature depicted in Fig. 11b negates any possibility of recrystallization for the current test conditions. This could be the reason behind no significant increase in the total elongation observed in the tensile flow curves with increasing temperature and decreasing strain rates. This is consistent with the intricate interplay of variables such as pre-existing strain, strain rate, processing-induced strain, and temperature, all of which contribute to the recrystallization process [66].

7 Conclusions

A flow behavior investigation was conducted on a 1 mm sheet of AA5052 alloy through isothermal uniaxial tensile tests, adhering to ASTM E-8 standards. The study encompassed a spectrum of strain rates spanning from 0.001 to 0.1 s⁻¹, as well as temperatures ranging from room temperature to 300 °C. The predictive accuracy of three distinct models—Johnson–Cook, Modified Arrhenius, and BP-ANN—was juxtaposed and evaluated. To establish a correlation between structure and properties, EBSD analysis was performed on tensile samples strained to 17% under various testing conditions. This correlation aimed to shed light on the interrelationship between material microstructure and its mechanical response.

The key conclusions drawn from this study are as below:

- i. The flow curve depicted an inverse sensitivity with test temperature however, very little positive sensitivity was observed for strain rate (at higher temperatures).
- ii. Serrations of Type-B were noted at lower temperatures, specifically within the range of 25–200 °C, across all strain rates spanning from 0.001 to 0.1 s⁻¹.

- iii. K–M plot for strain hardening rate (θ) and net flow stress ($\sigma - \sigma_y$) shows the presence of stage-III and Stage V at all test conditions however, stage IV was observed only for low temperatures of 25–100 °C.
- iv. ANN model gave much better prediction of flow stress wrt. J–C and Modified Arrhenius model with ARRE values of 1.77%, 3.42% and 4.26%, respectively.
- v. KAM analysis revealed the presence of dynamic recovery for lowest strain rate of 0.001 s⁻¹ resulting into relatively clearer microstructure with lower sub-grain.

Acknowledgements The authors would like to extend our sincere gratitude to the management of Aditya Birla Science & Technology Co. Pvt. Ltd., Navi Mumbai, for their generous sponsorship of the ongoing PhD research. We are truly grateful to Prof. M.J.N.V. Prasad, MEMS Dept (IIT Bombay), for his continuous guidance and invaluable advices throughout this research work. We would also like to express our deep appreciation to Dr. Soumyaranjan Nayak, Metal Forming lab, (IIT Bombay) for his insightful and constructive discussions during the research.

Declarations

Conflict of Interest Authors do not have any conflicts with individuals or authorities, and they retain full ownership of the research idea and its outcomes. Consequently, we affirm that the article is entirely original. It has been authored by the individuals specified, all of whom are fully knowledgeable about its content and endorse its submission. The article has not been previously published, nor is it currently under consideration for publication elsewhere. There are no conflicts of interest to declare.

References

1. E. Bumiller, Intergranular corrosion in AA5XXX aluminum alloys with discontinuous precipitation at the grain boundaries, Ph. D.

- Thesis, University of Virginia (2011). <https://www.proquest.com/docview/903291978>
2. M.L.C. Lim, R.G. Kelly, J.R. Scully, *Corrosion* **72**, 198 (2016). <https://doi.org/10.5006/1818>
 3. F. Ozturk, S. Toros, S. Kilic, *Arch. Mater. Sci. Eng.* **34**, 95 (2008)
 4. R. Liang, A.S. Khan, *Int. J. Plast.* **15**, 963 (1999). [https://doi.org/10.1016/S0749-6419\(99\)00021-2](https://doi.org/10.1016/S0749-6419(99)00021-2)
 5. Z. Gronostajski, *J. Mater. Process. Technol.* **106**, 40 (2000). [https://doi.org/10.1016/S0924-0136\(00\)00635-X](https://doi.org/10.1016/S0924-0136(00)00635-X)
 6. H.J. McQueen, *Metall. Mater. Trans. A* **33**, 345 (2002). <https://doi.org/10.1007/s11661-002-0096-3>
 7. T. Sakai, A. Belyakov, R. Kaibyshev, H. Miura, J.J. Jonas, *Prog. Mater. Sci.* **60**, 130 (2014). <https://doi.org/10.1016/j.pmatsci.2013.09.002>
 8. C. Zener, J.H. Hollomon, *J. Appl. Phys.* **15**, 22 (1944). <https://doi.org/10.1063/1.1707363>
 9. C.M. Sellars, W.J. McTegart, *Acta Metall.* **14**, 1136 (1966). [https://doi.org/10.1016/0001-6160\(66\)90207-0](https://doi.org/10.1016/0001-6160(66)90207-0)
 10. G.R. Johnson, W.H. Cook, in *Proceedings of the 7th International Symposium on Ballistics*, The Hague, 19-21 April 1983 (1983). pp. 541–547
 11. F.J. Zerilli, R.W. Armstrong, *J. Appl. Phys.* **61**, 1816 (1987). <https://doi.org/10.1063/1.338024>
 12. C.M. Sellars, *Czechoslov. J. Phys. B* **35**, 239 (1985). <https://doi.org/10.1007/BF01605090>
 13. J.H. Guo, S.D. Zhao, G.H. Yan, Z.B. Wang, *Mater. Sci. Technol.* **29**, 197 (2013). <https://doi.org/10.1179/1743284712Y.0000000140>
 14. J. Guo, S. Zhao, R. Murakami, R. Ding, S. Fan, *J. Alloys Compd.* **566**, 62 (2013). <https://doi.org/10.1016/j.jallcom.2013.03.022>
 15. C.D. Lee, *Met. Mater. Int.* **14**, 15 (2008). <https://doi.org/10.3365/met.mat.2008.02.015>
 16. J. Guo, Y. Li, H. Ding, in *Proceedings of the 6th International Conference on Manufacturing Science and Engineering*. Guangzhou, 28-29 November 2015 (Atlantis Press, Dordrecht, 2015). <https://doi.org/10.2991/icmse-15.2015.168>
 17. P. Song, W. Li, X. Wang, W. Xu, *Mater. Sci. Technol.* **35**, 916 (2019). <https://doi.org/10.1080/02670836.2019.1596611>
 18. H. Huh, W.J. Kang, S.S. Han, *Exp. Mech.* **42**, 8 (2002). <https://doi.org/10.1007/BF02411046>
 19. C.Y. Gao, L.C. Zhang, *Int. J. Plast.* **32**, 121 (2012). <https://doi.org/10.1016/j.ijplas.2011.12.001>
 20. J. Cai, F. Li, T. Liu, B. Chen, M. He, *Mater. Des.* **32**, 1144 (2011). <https://doi.org/10.1016/j.matdes.2010.11.004>
 21. C.R. Anoop, A. Prakash, S.K. Giri, S.V.S.N. Murty, I. Samajdar, *Mater. Charact.* **141**, 97 (2018). <https://doi.org/10.1016/j.matchar.2018.04.025>
 22. L. Li, L. Wang, *High Temp. Mater. Process.* **37**, 411 (2018). <https://doi.org/10.1515/htmp-2016-0234>
 23. S. Nayak, P. Dhondapure, A.K. Singh, M. Prasad, K. Narasimhan, *Adv. Mater. Process. Technol.* **6**, 244 (2020). <https://doi.org/10.1080/2374068X.2020.1731233>
 24. G. Xiao, Q. Yang, L. Li, J. Zeng, *Met. Mater. Int.* **22**, 58 (2016). <https://doi.org/10.1007/s12540-015-5296-7>
 25. D. Jiang, J. Zhang, T. Liu, W. Li, Z. Wan, T. Han, C. Che, *L. Cheng, Metals* **12**, 1787 (2022). <https://doi.org/10.3390/met12111787>
 26. H.R. Ashtiani, P. Shahsavari, *Trans. Nonferrous Met. Soc. China* **30**(11), 2927 (2020). [https://doi.org/10.1016/S1003-6326\(20\)65432-2](https://doi.org/10.1016/S1003-6326(20)65432-2)
 27. H.R. Rezaei Ashtiani, A.A. Shayanpoor, *Met. Mater. Int.* **27**, 5017 (2021). <https://doi.org/10.1007/s12540-020-00943-y>
 28. E. Pu, W. Zheng, J. Xiang, Z. Song, J. Li, *Mater. Sci. Eng. A* **598**, 174 (2014). <https://doi.org/10.1016/j.msea.2014.01.027>
 29. V. Tari, A.D. Rollett, H. Beladi, *J. Appl. Crystallogr.* **46**, 210 (2013). <https://doi.org/10.1107/S002188981204914X>
 30. L. Kestens, J.J. Jonas, in *ASM Handbook, Vol. 14A, Metalworking: Bulk Forming*, ed. by S.L. Semiatin (ASM International, Materials Park, 2005), p. 685
 31. G.E. Dieter, H.A. Kuhn, S.L. Semiatin, *Handbook of Workability and Process Design* (ASM International, Materials Park, 2003)
 32. C.M. Sellars, W.J.M. Tegart, *Int. Metall. Rev.* **17**, 1 (1972). <https://doi.org/10.1179/imtr.1972.17.1.1>
 33. Y.C. Lin, X.-M. Chen, *Mater. Des.* **32**, 1733 (2011). <https://doi.org/10.1016/j.matdes.2010.11.048>
 34. Z. Zeng, S. Jonsson, Y. Zhang, *Mater. Sci. Eng. A* **505**, 116 (2009). <https://doi.org/10.1016/j.msea.2008.11.017>
 35. A.A. Khamei, K. Dehghani, *J. Alloys Compd.* **490**, 377 (2010). <https://doi.org/10.1016/j.jallcom.2009.09.187>
 36. G.R. Johnson, W.H. Cook, *Eng. Fract. Mech.* **21**, 31 (1985). [https://doi.org/10.1016/0013-7944\(85\)90052-9](https://doi.org/10.1016/0013-7944(85)90052-9)
 37. Y. Zhang, J.C. Outeiro, T. Mabrouki, *Proc. CIRP* **31**, 112 (2015). <https://doi.org/10.1016/j.procir.2015.03.052>
 38. G. Prakash, N.K. Singh, P. Sharma, N.K. Gupta, *J. Mater. Civ. Eng.* **32**, 04020090 (2020). [https://doi.org/10.1061/\(ASCE\)MT.1943-5533.0003154](https://doi.org/10.1061/(ASCE)MT.1943-5533.0003154)
 39. M. Grujicic, B. Pandurangan, C.-F. Yen, B.A. Cheeseman, *J. Mater. Eng. Perform.* **21**, 2207 (2012). <https://doi.org/10.1007/s11665-011-0118-7>
 40. B.J. Brindley, P.J. Worthington, *Metall. Rev.* **15**, 101 (1970). <https://doi.org/10.1179/mtr.1970.15.1.101>
 41. C.-H. Cho, H.-W. Son, J.-C. Lee, K.-T. Son, J.-W. Lee, S.-K. Hyun, *Mater. Sci. Eng. A* **779**, 139151 (2020). <https://doi.org/10.1016/j.msea.2020.139151>
 42. T. Brynk, K.J. Kurzydowski, *Scr. Mater.* **174**, 14 (2020). <https://doi.org/10.1016/j.scriptamat.2019.08.024>
 43. K. Chihab, Y. Estrin, L.P. Kubin, J. Vergnol, *Scr. Metall.* **21**, 203 (1987). [https://doi.org/10.1016/0036-9748\(87\)90435-2](https://doi.org/10.1016/0036-9748(87)90435-2)
 44. D. Delpueyo, X. Balandraud, M. Grédiac, *Mater. Sci. Eng. A* **651**, 135 (2016). <https://doi.org/10.1016/j.msea.2015.10.053>
 45. N. Tian, W. Wang, Z. Feng, W. Song, T. Wang, Z. Zeng, G. Zhao, *G. Qin, Materials* **15**, 4965 (2022). <https://doi.org/10.3390/ma15144965>
 46. Q. Hu, Q. Zhang, S. Fu, P. Cao, M. Gong, *Theor. Appl. Mech. Lett.* **1**, 011007 (2011). <https://doi.org/10.1063/2.1101107>
 47. F.B. Klose, A. Ziegenbein, F. Hagemann, H. Neuhäuser, P. Hähner, M. Abbadi, A. Zeghloul, *Mater. Sci. Eng. A* **369**, 76 (2004). <https://doi.org/10.1016/j.msea.2003.10.292>
 48. L.P. Kubin, Y. Estrin, *J. de Phys. III* **1**, 929 (1991). <https://doi.org/10.1051/jp3:1991166>
 49. G.E. Dieter Jr, *Mechanical Metallurgy* (McGraw Hill, New York, 1961), pp. 81–117
 50. A. Sarkar, S.V.S.N. Murty, M. Prasad, *Metall. Mater. Trans. A* **51**, 4742 (2020). <https://doi.org/10.1007/s11661-020-05892-0>
 51. T. Kazaoka, D.H. Zhou, N. Kataoka, R. Matsumoto, H. Utsunomiya, *Adv. Mat. Res.* **922**, 344 (2014). <https://doi.org/10.4028/www.scientific.net/AMR.922.344>
 52. J. Wu, F. Djavaeroodi, C. Gode, M. Ebrahimi, S. Attarilar, *Mater. Res. Expr.* **9**, 056516 (2022). <https://doi.org/10.1088/2053-1591/ac6b8d>
 53. R. Fu, Y. Huang, Y. Liu, H. Li, *Met. Mater. Int.* **29**, 2605 (2023). <https://doi.org/10.1007/s12540-023-01397-8>
 54. W. Abdel-Aziem, A. Hamada, T. Makino, M.A. Hassan, *Met. Mater. Int.* **27**, 1756 (2021). <https://doi.org/10.1007/s12540-019-00544-4>
 55. K.-T. Son, J.-W. Lee, T.-K. Jung, H.-J. Choi, S.-W. Kim, S.K. Kim, Y.-O. Yoon, S.-K. Hyun, *Met. Mater. Int.* **23**, 68 (2017). <https://doi.org/10.1007/s12540-017-6384-7>
 56. E. Vaghefi, S. Serajzadeh, *Met. Mater. Int.* **27**, 4368 (2021). <https://doi.org/10.1007/s12540-020-00755-0>

57. G. Chen, G. Fu, H. Chen, C. Cheng, W. Yan, S. Lin, *Met. Mater. Int.* **18**, 813 (2012). <https://doi.org/10.1007/s12540-012-5010-y>
58. D.H. Jang, W.J. Kim, *Met. Mater. Int.* **24**, 455 (2018). <https://doi.org/10.1007/s12540-018-0061-3>
59. C. Li, G. Huang, L. Cao, R. Zhang, Y. Cao, B. Liao, L. Lin, *Met. Mater. Int.* **28**, 1561 (2022). <https://doi.org/10.1007/s12540-021-01025-3>
60. W. Abdel-Aziem, M.A. Hassan, T. Makino, A. Hamada, *Metallogr. Microstruct. Anal.* **10**, 402 (2021). <https://doi.org/10.1007/s13632-021-00753-7>
61. S.I. Wright, M.M. Nowell, D.P. Field, *Microsc. Microanal.* **17**, 316 (2011). <https://doi.org/10.1017/S1431927611000055>
62. E. Nes, K. Marthinsen, Y. Brechet, *Scr. Mater.* **47**, 607 (2002). [https://doi.org/10.1016/S1359-6462\(02\)00235-X](https://doi.org/10.1016/S1359-6462(02)00235-X)
63. A. Kumar, A. Shrivastava, K. Narasimhan, S. Mishra, *J. Mater. Sci.* **57**, 6368 (2022). <https://doi.org/10.1007/s10853-022-07036-8>
64. B. Liao, L. Cao, X. Wu, Y. Zou, G. Huang, P.A. Rometsch, M.J. Couper, Q. Liu, *Materials* **12**, 311 (2019). <https://doi.org/10.3390/ma12020311>
65. A.D. Rollett, M. Alvi, A. Brahme, J. Fridy, H. Weiland, J. Suni, S. Cheong, Texture-dependent recrystallization in aluminum 1050, in *Proceedings of the 9th International Conference on Aluminium Alloys*, ed. by J.F. Nie, A.J. Morton, B.C. Muddle. ICAA9, Brisbane, 2-5 August 2004 (Institute of Materials Engineering Australasia Ltd, Melbourne, 2004), p. 1173
66. W.D. Callister Jr, *Materials Science and Engineering: An Introduction*, 7th edn. (John Wiley & Sons, New York, 2007), pp. 216–250

Publisher's Note Springer Nature remains neutral with regard to jurisdictional claims in published maps and institutional affiliations.

Springer Nature or its licensor (e.g. a society or other partner) holds exclusive rights to this article under a publishing agreement with the author(s) or other rightsholder(s); author self-archiving of the accepted manuscript version of this article is solely governed by the terms of such publishing agreement and applicable law.